Atmos. Chem. Phys. Discuss., 10, 12907–12952, 2010
www.atmos-chem-phys-discuss.net/10/12907/2010/
doi:10.5194/acpd-10-12907-2010

Atmospheric Chemistry and Physics Discussions

Detailed cloud resolving model simulations of the impacts of Saharan air layer dust on tropical deep convection – Part 1: Dust acts as ice nuclei

W. Gong[1], Q. Min[1], R. Li[1], A. Teller[2], E. Joseph[3], and V. Morris[3]

[1]Atmospheric Sciences Research Center, State University of New York at Albany, 251 Fuller Rd, Albany, New York 12203, USA
[2]Energy, Environment and Water Research Center, The Cyprus Institute, Nicosia, Cyprus
[3]NOAA Center for Atmospheric Sciences, Howard University Washington, DC 20001, USA

Received: 26 January 2010 – Accepted: 26 April 2010 – Published: 19 May 2010

Correspondence to: W. Gong (wgong@climate.cestm.albany.edu)

Published by Copernicus Publications on behalf of the European Geosciences Union.

Abstract

Observational studies suggest that the Saharan Air Layer (SAL), an elevated layer (850–500 hPa) of Saharan air and mineral dust, has strong impacts on the microphysical as well as dynamical properties of tropical deep convective cloud systems along its track. In this case study, numerical simulations using a two-dimensional Detailed Cloud Resolving Model (DCRM) were carried out to investigate the dust-cloud interactions in the tropical deep convection, focusing on the dust role as Ice Nuclei (IN).

The simulations showed that mineral dust considerably enhanced heterogeneous nucleation and freezing at temperatures warmer than −40 °C, resulting in more ice hydrometeors number concentration and reduced precipitating size of ice particles. Because of the lower in the saturation over ice as well as more droplet freezing, total latent heating increased, and consequently the updraft velocity was stronger.

On the other hand, the increased ice deposition consumed more water vapor at middle troposphere, which induces a competition for water vapor between heterogeneous and homogeneous freezing and nucleation. As a result, dust suppressed the homogeneous droplet freezing and nucleation due to the heterogeneous droplet freezing and the weakened transport of water vapor at lower stratosphere, respectively. These effects led to decreased number concentration of ice cloud particles in the upper troposphere, and consequently lowered the cloud top height during the stratus precipitating stage.

Acting as IN, mineral dust also influenced precipitation in deep convection. It initiated earlier the collection because dust-related heterogeneous nucleation and freezing at middle troposphere occur earlier than homogeneous nucleation at higher altitudes. Nevertheless, the convective precipitation was suppressed by reduced collection of large graupel particles and insufficient fallout related to decreased sizes of precipitating ice hydrometeors. On the contrary, dust increased the precipitation in stratiform precipitation through deposition growth. Overall, the comprehensive effects of mineral dust suppressed the precipitation by up to 22%.

ACPD
10, 12907–12952, 2010

1 Introduction

Atmospheric mineral dust particles are among the most uncertain factors contributing to the effects of aerosols on global climate (IPCC, 2001). Desert regions of the Sahara are a major contributor to the total global dust annual production (Schütz et al., 1981; Ginoux et al., 2004). The mineral dust particles are transported long distances westward with the tropical winds, in an elevated layer of 850–500 hPa, known as Saharan Air Layer (SAL; Prospero and Carlson, 1970; Carlson and Prospero, 1972). In its pathway across the Atlantic Ocean, SAL interacts with tropical cloud systems, including Atlantic hurricanes, and may substantially influence their evolution and intensity (Karyampudi and Carlson, 1988; Dunion and Velden, 2004; Min et al., 2009).

Silicate particles, the main components of Saharan mineral dust, are primarily insoluble aerosols (Lohmann, 2002), and can serve as efficient Ice Nucleus (IN; Pruppacher and Klett, 1997; Demott et al., 2003; Sassen et al., 2003). During the transport, some of the insoluble particles are commonly found to attach with sea salt or anthropogenic pollutants, such as sulfate and nitrate. These coatings may cause the mineral dust particles to be more soluble and increase their chance to serve as Cloud Condensate Nucleus (CCN; Levin et al., 1996; Trochkine et al., 2003; Semeniuk et al., 2007). As a result, mineral dust may affect clouds directly through their heterogeneous nucleation into ice crystals and/or activation into cloud drops. With these additional cloud condensates, mineral dust may have impacts on the tropical deep convective clouds in the following three aspects: cloud macrophysical- and microphysical- properties, such as cloud optical depth, spatial coverage, and effective radius associated with number concentration and size distribution of cloud condensates (Min and Li, 2010a); precipitation including surface precipitation and vertical structure; and cloud dynamic and thermodynamic structures.

A recent observational study (Min et al., 2009) indicated that the ice particles are abundant in the dust sector of the tropical deep convection, especially at altitudes where heterogeneous ice nucleation prevails, and consequently the effective radius

ACPD
10, 12907–12952, 2010

is reduced. At the same time, the height of cloud top is lowered because more ice hydrometeors are formed through heterogeneous ice nucleation and consume more water vapor. Therefore homogeneous nucleation at higher altitudes has less water vapor supply, leading to reduced homogeneous nucleation. The macrophysical changes in ice cloud top distributions as a consequence of mineral dust-cloud interaction exert a strong cooling effect (up to 16 Wm^{-2}) of thermal infrared radiation on cloud systems (Min and Li, 2010a). Model simulations suggest that dust aerosols increase the number concentration of ice (Khain et al., 2009), and ice water depth, and decrease the cloud cover (Lohmann and Diehl, 2006). On the other hand, with higher number concentration of cloud drops, the growth of cloud condensates will change, leading to smaller cloud droplet sizes, larger optical depth (Twomey, 1977), and longer cloud lifetime (Albrecht, 1989).

Numerous studies suggest that mineral dust is of great importance in precipitation development albeit there are no conclusive results on whether dust enhances or suppresses precipitation. Rosenfeld et al. (2001) suggested that mineral dust coated with sulfate acting as CCN reduces the size of the cloud droplet and consequently suppresses and delays the warm rain process due to the reduction of cloud drop collection efficiency. Dust particles can also act as giant CCNs (GCCN) to affect precipitation, but still with large degrees of uncertainties in the conclusion. Modeling studies (Levin et al., 2005; Teller and Levin, 2006) demonstrated that acting as GCCN mineral dust enhances precipitation by producing large cloud drops. On the other hand, the simulations of Posselt and Lohmann (2009) suggested that GCCN does not change the total precipitation, and instead it only accelerates the hydrological cycle so that clouds precipitate faster and less condensed water is accumulated in the atmosphere. It should be noted that those simulations were carried out in low spatial resolution using GCM. Nevertheless, simulations of van den Heever et al. (2006) suggested dust suppresses the accumulate precipitation in tropical storms. An additional observational study by Min et al. (2009) found that SAL mineral dust shifts the size spectrum from heavy precipitation to light and ultimately suppresses the precipitation in convective clouds.

ACPD
10, 12907–12952, 2010

In addition to the precipitation, there are uncertainties in the dust impacts on the dynamics of tropical deep convection system. A modeling study of van den Heever et al. (2006) suggested that dust particles will substantially enhance the vertical updraft velocity due to the increased latent heat release associated with the production of drop and ice hydrometeors, no matter whether they act as CCN, GCCN, IN or their mixtures. On the contrary, in simulations of Khain et al. (2009) the intensity of tropical cyclone was significantly weakened by the continental aerosol acting as CCN.

In this study, we investigated the SAL mineral dust impact on tropical deep convection, using a Detailed Cloud Resolving Model (DCRM) with detailed description of warm and cold cloud microphysics. Our objectives are twofold. First, the conclusions of the dust effects on tropical deep convection drawn in the observational studies of Min et al. (2009) could be interfered with the noises induced by the difference in dynamic and thermodynamic variations, although tremendous efforts have been done in their analysis to isolate the impacts of dust aerosols. On the other hand, the advantage of model simulations is the capability to separate influences of dynamical and cloud microphysics , and therefore the model can offer confirmation on the analysis of Min et al. (2009). Second, model outputs, including all cloud condensates and tendencies due to all physical processes at various spatial, time and size scales can provide detailed information for understanding the mechanisms how mineral dust impacts the tropical deep convective clouds.

Below in Sect. 2, we give a description of the DCRM, along with recent updates of the parameterizations of cold cloud microphysics, in addition to a description of the experiment design. The generated deep convective clouds are nearly symmetric, without initial horizontal wind, and thus it is feasibly for us to understand the dust-cloud interactions, while the simulations with initial horizontal wind will be more realistic. Therefore, we present in Sects. 3 and 4 the results of dust acting as IN, without and with initial horizontal wind, respectively. The summary and discussion are given in Sect. 5.

ACPD
10, 12907–12952, 2010

2 Model description and experiments design

2.1 Model description

2.1.1 Overview

The model simulations were carried out with a DCRM, developed at Tel Aviv University. DCRM is a two-dimensional slab-symmetric non-hydrostatic cloud model (Yin et al., 2000; Yin and Chen, 2007) that makes use of the spectral method of moments for calculating the change in the distribution of hydrometeors (Tzivion et al., 1987; Reisin et al., 1996). The vertical and horizontal velocities and perturbations of surface pressure, virtual potential temperature and specific water vapor are dynamical and thermaldynamical prognostic variables, respectively. Other predicting variables in the model are specific concentration of CCN and IN, the specific mass and four species of cloud condensates (drops, graupel, ice crystals, and snowflakes).

Based on Reisin et al. (1996), the aerosols and hydrometers equations are solved in spectral bins. In this study we use 48 spectral bins for the aerosols and 34 bins for hydrometeors, similar to Yin and Chen (2007). Both diameters of CCN and IN range from 0.11 to 32 µm. Mass doubling categories are divided for adjacent bins of hydrometeors, and their lower and upper bin boundaries are the same as Yin et al. (2005).

The DCRM has been used in many applications, specializing on CCN generated clouds. The warm cloud microphysical processes consider drop nucleation of CCN, condensation/evaporation, collision-coalescence, and binary break-up. The CCN coating is assumed to be sulfate although sea salt is also a major coating for aerosol over the ocean. Drop nucleation is based on supersaturation and critical diameter following the Köhler theory (Pruppacher and Klett, 1997).

In previous model versions, the forming of ice hydrometeors considers deposition nucleation and contact freezing (Meyers et al., 1992), and immersion freezing (Bigg, 1953) when drops contain activated IN. The concentration of activated IN is propor-

ACPD
10, 12907–12952, 2010

tional to supersaturation for deposition nucleation, and to supercooling temperature for contact freezing. Ice multiplication (H-M process; Hallet and Mossop, 1974) induced by collisions of large drops and ice particles is also a source of ice hydrometeors.

Interactions of ice-ice and ice-drop interaction (aggregation, accretion and riming), and sedimentation are considered. Ice particles grow by deposition and aggregation to form snowflakes and by riming to form graupel. After large ice particles fall below freezing level, they melt to form raindrops. Large raindrops collide with other raindrops and break up to become smaller drops based on the work of Reisin et al. (1998).

2.1.2 Heterogeneous ice nucleation and freezing schemes

As described previously, the parameterizations of deposition nucleation and contact freezing (Meyers et al., 1992) do not relate the nucleation rate to dust number concentration, explicitly. Therefore, in the DCRM we updated the parameterizations for these two ice forming processes.

According to van den Heever et al. (2006), we assumed that the number of pristine ice crystals generated by deposition nucleation (N_{hen}) is proportional to the IN number concentration (N_{IN}; l^{-1}):

$$N_{hen} = N_{IN} F_M \quad (1)$$

where F_M (unitness) is a function of the deposition nucleation by Meyers et al. (1992) that represents the fraction of available IN (Nid; l^{-1}):

$$\text{Nid} = \exp\{-6.39 + 0.1296[100(S_i - 1)]\} \quad (2)$$

with S_i the saturation over ice. F_M is maximized (equal to 1) for condition at the ice supersaturation of 40%, at which all the IN are being activated, and is equal to 0 when supersaturation over ice is negative. The initial size of nucleated pristine ice crystal is assumed to be 2.5 µm in radius as in Yin et al. (2007).

We adopted the contact freezing scheme of Muhlbauer and Lohmann (2009). In the parameterization, the contact freezing is induced by collision of supercooled liquid wa-

ACPD
10, 12907–12952, 2010

ter drops and IN due to Brownian motion. As a result, the freezing rate is proportional to the drops radius and number concentration. It is also proportional to the IN number concentration and Brownian diffusivity in air. Unlike Muhlbauer and Lohmann (2009) who calculated the freezing rate for lump of all drops, we perform the calculation for each spectral bin of drops. Then the contact freezing rate (N_{cnt}; $l^{-1}\,s^{-1}$) for individual spectral bin is:

$$N_{cnt} = 4\pi r_C N_C D N_{IN} \tag{3}$$

where r_C (m) and $N_C(m^{-3})$ is radius and number concentration of drops, respectively. D the dust aerosol Brownian diffusivity ($m^2\,s^{-1}$), and is parameterized as:

$$D_k = \frac{k_B T C}{6\pi\eta r} \tag{4}$$

D_k is a function of Boltzmann constant K_k=1.28 $\times 10^{-23}\,m^2\,kg\,s^{-2}\,K^{-1}$, T is the air temperature, $r$is the dry dust aerosol median radius,η is the viscosity of air and C is the Cunningham slip correction factor. The viscosity of air depends on temperature:

$$\eta = 10^{-5}[1.718 + 4.9\times 10^{-3}(T-273.15) - 1.2\times 10^{-5}(T-273.15)^2] \tag{5}$$

The Cunningham slip correction factor is given by

$$C = 1 + 1.26\left(\frac{\lambda}{r}\right)\left(\frac{1013.25}{p}\right)\left(\frac{T}{273.15}\right) \tag{6}$$

with the molecular mean free path length of air λ=0.066 µm, and p is the pressure. To simplify the calculation the number of contact freezing number is the available dust number concentration N_{IN}, with freezing efficiency of 1. According to Yin et al. (2005), drops with radius smaller than 79.37 µm (18th bin) will be frozen to pristine ice crystal, otherwise to graupel.

ACPD
10, 12907–12952, 2010

2.1.3 Homogeneous ice nucleation and freezing schemes

Tropical deep convection frequently shoots up to stratosphere above 11 km where the temperature is colder than −40 °C, and hence homogeneous ice nucleation and freezing must be included in the model. For homogeneous ice nucleation, we implemented the parameterization (Liu and Penner, 2005) derived from the statistics of their parcel model simulations. This parameterization treats homogeneous nucleation by CCN coated with sulfate and deposition nucleation as described by Meyers et al. (1992) formulation. In addition to the pure sulfate aerosol number concentration, the scheme includes the effects of updraft velocity (w) and temperature under critical relative humidity threshold with respect to water

$$\mathrm{RH_w} = AT^2 + BT + C \tag{7}$$

where $A = 6\times10^{-4}\ln w + 6.6\times10^{-3}$, $B = 6\times10^{-2}\ln w + 1.052$, and $C = 1.68\ln w + 129.35$. As reported by Liu and Penner (2005), this critical $\mathrm{RH_w}$ is within 10% of the laboratory data of Koop et al. (1998) in the temperature range from −35° to −60 °C.

The growth of pristine ice crystals was divided into slow (colder T and faster w) and fast growth (warmer T and slower w) regimes, depending on the air mass temperature and updraft velocity. The critical temperature for the fast-growth regime was set to $T = 6.07\ln w - 55.0$, below that value the slow-growth regime was used. For the fast-growth regime the nucleated ice number concentration was

$$N_{\mathrm{hon}} = \exp(a_2 + (b_2 + b_3\ln w)T + c_2\ln w)N_{\mathrm{CCN}}^{a_1+b_1T+c_1\ln w} \tag{8}$$

and for the slow-growth regime, we used

$$N_{\mathrm{hon}} = \exp[a_2 + (b_2 + b_3\ln w)T + c_2\ln w]N_{\mathrm{CCN}}^{a_1+b_1T+c_1\ln w} \tag{9}$$

where N_{CCN} is CCN number concentration, and the coefficients are given in Table 1 of Liu et al. (2007). The initial size of nucleated pristine ice crystal was also assumed to be 2.5 μm in radius.

ACPD
10, 12907–12952, 2010

We incorporated the parameterization of Heymsfield and Milosevich (1993) to account for the homogeneous droplet freezing. This parameterization calculates the homogeneous freezing rate from the drop number concentration and temperature, for drop temperature colder than −50 °C. As described in Demott et al. (1994), the number concentration N_{hon_c} due to homogeneous freezing in time step Δt_c was

$$N_{\text{hon}} = \int_0^{\infty} [1 - \exp(-J_{\text{ls0}} \frac{4\pi r_c^3}{3} \Delta t)] N_c(r_c) dr_c \quad (10)$$

where r_c is drop radius and J_{ls0} is the nucleation rate for pure water, which is primarily a function of drop temperature (T_d), and can be approximated as (Heymsfield and Milosevich, 1993)

$$J_{\text{ls0}} = 10^y \quad (11)$$

with

$$y = -606.3952 - 52.6611 T_c - 1.7439 T_c^2 - 0.0265 T_c^3 - 1.536 \times 10^{-4} T_c^4 \quad (12)$$

with $T_c = T_d - 273$ (°C). Again, when drop size is smaller than 79.37 μm, the drop becomes pristine ice crystal, otherwise it becomes graupel.

2.2 Experiment design

The Saharan dust plume has a large spatial coverage and heavy loading over uniform open-oceans, which provides ideal cases for studying dust effect. The aim of our study is to examine the cloud-dust interactions in terms of mechanism, but not to reproduce the observed quantities. We selected the case of the beginning of March 2004, as used in the observational study by Min et al. (2009). In this case, the Saharan dust transported over the Atlantic along with a cloud system, in which portions of the cloud system interacted with the Saharan dust plume. Aerosol measurements were taken during the trans-Atlantic Aerosol and Ocean Science Expeditions (AEROSE) experiment (Morris et al., 2006). Unfortunately, there was no sounding data available under

ACPD
10, 12907–12952, 2010

cloudy conditions. As a substitute, we selected a similar tropical deep convection case over the Atlantic Ocean, taken on July 1 2006, from the AEROSE-2006 experiment. The satellite image of Meteosat 8 indicates that shallow convective activity emerged around at 03:00 UTC, developed into deep convection at around 12:00 UTC, and at around 21:00 UTC became stratiform precipitation. We used the cruise sounding data at 19:31 UTC as the initial thermal-dynamical condition, which represents an after-storm situation. This sounding was selected because other sounding data at previous hours were so dry in the upper troposphere causing cloud condensates transported with the updraft to experience evaporation and even to vanish at lower stratosphere during the integration.

Note that our understanding of the impact mechanism of mineral dust was not affected by the fact that the observations of mineral dust size distribution and the meteorological conditions did not occur on the same day. In fact, many cloud resolving model studies (such as Yin et al., 2000; Teller and Levin, 2006) used hypothetical or theoretical atmospheric thermodynamic profiles and aerosol measurements to study the aerosol effects.

To understand the dust-cloud interaction, we conducted two pairs of experiments, without and with horizontal wind. In each pair, we use the temperature and dew point temperature as the initial condition (Fig. 1a). This sounding has moist air (relative humidity >60%) below 6 km and between 10–14 km, and very dry air (relative humidity <30%) between 8–11 km. For each pair of simulations, dust-free and dust initial conditions are simulated. The dust-free and dust cases are denoted as Cases F and D, respectively, while a supplementary letter *U* denotes pairs with horizontal wind. For example, Case FU refers to the dust-free case simulated under the circumstance of horizontal wind.

Table 1 presents the cruise measurement of number concentrations of aerosol on dust-free and dust day in March 2004. The data needs to be interpolated to each model bins as input of initial conditions at the surface level. In this study, we simplified the aerosol data processing by assuming that the differences between the two mea-

ACPD
10, 12907–12952, 2010

surements are the dust loading. The measurement at aerosol size 0.3–0.5 µm on the dust-free day has a larger number concentration (108.6 cm^{-3}) than the corresponding dust day (87.32 cm^{-3}), therefore the dust loading is calculated for sizes greater than 0.5 µm. The dust layer is assumed to be between 1 and 3 km (913 and 710 hPa). Because the SAL is usually located between 850 and 500 hPa, the altitudes in the simulations are a little bit lower, which is more close to the cruise measurement at sea level. The background CCN number concentration in the dust-free runs was derived from the measurements on the dust free-day. In the calculation, we linearly interpolated the number concentration to each bin, although many studies use multi-mode fitting under assumption of lognormal distribution (e.g., Yin and Chen, 2007).

As in Yin et al. (2005), we also assumed a uniform aerosol vertical distribution (for both CCN and IN) within the maritime planetary boundary layer with depth of 1000 m, and exponentially decreasing vertical distribution above the layer, using the following relationship:

$$[A(z)] = [A(z_0)]\exp[-(z - z_0)/H] \quad (13)$$

where $[A]$ is the aerosol number concentration, z is the height of model levels, z_0 the planetary boundary layer height (1000 m), and H (1500 m) the scale height for the exponential decrease profile. According to DeMott et al. (2006), the background IN number concentration {[IN]} is derived from an empirical power-law relationship between number concentration of IN and CCN:

$$[\mathrm{IN}] = 4.8828[\mathrm{CCN}]^{1.4505} \quad (14)$$

More information on the IN vertical distribution will be presented in Sect. 3. For comparison, we also conducted simulations with a vertically uniform profile of background IN as used in van den Heever et al. (2006). The conclusions of simulated dust effects were not modified with different values of background IN.

The model domain set-up was designed to simulate a single cell cloud. The grid size in both horizontal and vertical directions was 300 m, as used in Yin and Chen (2007).

ACPD
10, 12907–12952, 2010

The corresponding grid numbers were 301 and 80, which represented a 90 km wide and 24 km height domain, respectively. Time step was set to 2 s, while 1 s was used for deposition/condensation processes. The model was integrated for 100 min (after that time the cloud almost disappeared except at lateral boundaries).

The DCRM has been used in many case studies, but in most of them the simulated cloud tops were not higher than 10 km. In our case study, the tops of observed tropical deep convection frequently reach 14 km or higher. In order to study the competition for water vapor between heterogeneous and homogeneous nucleation, it was critical to let the convection shoot above the levels below −40 °C where homogeneous nucleation can take place. Special treatments were used to reach this goal. First, as in Yin and Chen, a 2 °C initial (one time step) potential temperature perturbation was applied at two bottom levels at domain center (149–151 grids). Second, following Wu and Moncrieff (1996), a time-dependent potential temperature perturbation (θ'; °C) forcing was applied at the 11 horizontal grids at the domain center and at the model levels below 4.5 km, with the form:

$$\theta' = 0.1t \leq 15 \text{ min}, \quad \theta' = 0.1 \cdot (30 - t)/1515 > t > 30 \text{ min} \tag{15}$$

where t is integration time in minutes. Above 4.5 km, the forcing is decreased linearly with height at a ratio of 0.85 between adjacent layers until the perturbation becomes zero. This thermal forcing provides planetary boundary sensible flux at lower levels and gradually decreases to zero to avoid numerical abortion. Third, it is mandatory to eliminate lateral boundary instability caused by high relative humidity. The sounding data of relative humidity was used as the initial condition at every model column except in the 30-grid buffer zones near lateral boundary. At the outermost lateral boundary, relative humidity was set to 15%, and was linearly interpolated to the initial relative humidity at 30th grid from the lateral boundary. Besides, as in the previous versions of DCRM an open lateral boundary condition was used.

ACPD
10, 12907–12952, 2010

3 Results without initial horizontal wind

With the applied thermal forcing, the control run (Case F) simulated convective cloud that was initiated quickly after the integration. At 2 min, a convective core was formed near height of 3 km, with updraft velocity above 5 m s^{-1}, and well-defined compensational downdrafts on both sides of the convective core. The core started in a region of about 3 km wide, and extended to about 8 km. At 18 min, the convection developed into its prosperous period. There was a maximum of updraft of 17 m s^{-1} at around 6 km, and the updraft had extended to the upper troposphere to 10 km. The convective bulb kept growing up to height of 15 km until 29 min. At around 35 min the convective core was broken at the middle troposphere at height of 8 km. After 40 min, a weak updraft of 1–2 m s^{-1} still prevailed at the altitudes between 8 and 15 km. It remained till 80 min, while weak up and down vertical motions fluctuated during the rest of the 20 min of integration.

In general, the model generated deep convection was similar to the deep convective clouds described in Min et al. (2009), and was in reasonable agreement with the classical description of tropical deep convection (e.g. Houze, 1993).

Based on the above description, we primarily presented the model results in two periods: *convective and stratiform precipitating stages*, which are also used in the observational study of Min et al. (2009). The first stage (0–39 min) is characterized by the strong updraft and severe precipitation with steep time changes in precipitation rate. The second (40–100 min) updraft is weak (typically ~1–2 m/s) and precipitation is weak but stable (Houze, 1993). Hereafter, we defined the *domain* as the grids between 100 and 200, with a width of about 30 km. Outside the domain, the simulations were contaminated by the secondary clouds generated at lateral boundaries after 70 min of integration. We also defined *convective core* as the grids between 140 and 160.

ACPD
10, 12907–12952, 2010

3.1 IN vertical distribution

Figure 2 shows vertical distribution (in logarithm scale; labels of x-axis denote the power of 10) in Cases F and D of IN number concentration at 1, 32 (late convective precipitating stage) and 100 min (late stratiform precipitating stage) in the domain. We only plotted the initial profile of the dust-free case at 1 min for Case F as there is no noticeable change in the IN number concentration , due to its small magnitudes above 5 km and due to the balance of small consumption of heterogeneous ice nucleation and freezing and dynamical transport. The dust layer, in which the number concentration of IN is 3 orders of magnitude higher than the dust free case, is located at 1–3 km and can be clearly seen at the beginning of integration.

The updraft in the convective precipitating stage efficiently transported the IN upward to upper troposphere as shown by the profile at 32 min. The increase of IN number concentration was still about 3 orders larger than the background throughout the troposphere. In fact, after 32 min the IN number concentration below 10 km has reached quasi-equilibrium between transport and consumption related to heterogeneous ice nucleation and freezing. Weak upward motion in the stratiform precipitating stage further carried the dust to the stratosphere as high as 16 km.

3.2 Size distribution change due to dust

The increased dust IN number concentration introduces considerable enhancement of heterogeneous ice nucleation processes under favorable moisture conditions. Figure 3a shows the heterogeneous ice nucleation rates of Case D averaged during convective and statiform precipitating stages in the convective core. The heterogeneous ice nucleation significantly increased due to the presence of dust (The heterogeneous nucleation and freezing rates are not shown for Case F, because they are very small). The heterogeneous nucleation occurs primarily near 5.8 km, relating to the hypothesis that all IN are fully nucleated if 140% ice supersaturation is reached. The ice nucleation rate at 6–10.8 km in the convective core has a peak around 20 min during the

ACPD
10, 12907–12952, 2010

convective precipitating stage.

The corresponding heterogeneous ice freezing rates are shown in Fig. 3b. For Case F, there are two maxima in the convective precipitating stage, one near 5 km and the other near 9 km. The lower level maximum is caused by contact freezing, while the higher level maximum is a result of immersion freezing, consistent with those described in Meyers et al. (1992) and Liu et al. (2005). In contrast to the heterogeneous nucleation, the immersion freezing rate is strongly time-dependent. The immersion freezing rate is negligible during stratiform precipitating stage. This result reflects the fact that supercooled drops have been frozen at the convective precipitating stage, and no further drop is transported to upper troposphere by the weak updraft during the stratiform precipitating stage.

On the other hand, drops are still transported to the middle troposphere by weak updraft so that contact freezing remains active during the stratiform precipitating stage. By comparing heterogeneous ice nucleation and freezing rates, we can see that the ice nucleation is the dominant process for ice number concentration at middle troposphere and is about 2 orders of magnitude larger than the ice freezing rates.

As there is huge increase in heterogeneous ice nucleation and freezing resulting from dust, the number concentration of ice hydrometeors should increase accordingly in ice saturation condition. At the same time, because the size of ice particles generated by heterogeneous nucleation is small, the growth of these ice particles will lead to change of the size spectrum.

Figure 4 shows the dust-induced changes in number concentration and mixing ratio of ice hydrometeors (ice and graupel) in the domain at upper troposphere and low stratosphere. At the altitudes of 6–10.8 km, where heterogeneous nucleation dominates, the number concentration of ice particles with size smaller than 0.503 mm is generally increased, except at 34–50 min where small size ice hydrometeors smaller than 0.107 mm decrease while a dipole pattern of changes occurs for size larger than this range.

The increase of number concentration of ice hydrometeors in the convective pre-

ACPD
10, 12907–12952, 2010

cipitating stage before 34 min is related to two factors. First, ice grows through the deposition process and the updraft carries sufficient water vapor. Second, the heterogeneous nucleation due to dust continuously generates new small ice particles.

To understand the changes of number concentration of ice hydrometeors between 34–50 min, we showed the vertical profile and time evolution of ice deposition rate for both Cases F and D in Fig. 5. Before 30 min, the depositional growth at the heights between 6.5 and 10 km in Case D more than doubles that in Case F. The enhancement of water vapor deposition consumes large amounts of water vapor (more discussion later), resulting in a dramatic decrease in growth at later times. In Case D ice sublimation occurs between 40–50 min, compared with continuous deposition in Case F. The combined effect of the decreased deposition and increased sublimation is responsible for the decrease of ice hydrometeors of smaller sizes.

At lower stratosphere between 11.1 and 14 km, dust increases the number concentration of ice hydrometeors before 25 min for all spectral bins and decreases the precipitating size particles larger than 0.503 mm after 40 min. In addition to the local deposition, homogeneous freezing nucleation and vertical transport by updraft of ice hydrometeors contribute to the change at these altitudes. The decrease of ice hydrometeors at smaller sizes results from the water vapor competition between heterogeneous and homogeneous nucleation.

Due to the increase of deposition growth, the water vapor is significantly reduced above 6 km between 20 and 60 min, as shown in Fig. 6. The mixing ratio peak at 11.1–14 km and at 35 min in Case D is reduced by more than half. The delayed peaks of water vapor at 11.1–14 km (compared to that of 6–10.8 km) as shown in Fig. 6a indicate that moisture is indeed brought upward by updraft.

As a result of the reduced water vapor, homogeneous nucleation is suppressed as shown by the vertical profile of homogeneous nucleation rate Fig. 7a, especially below 15 km. Note that the homogeneous nucleation at higher altitudes is associated with higher initial relative humidity taken from sounding data. On the other hand, the homogeneous droplet freezing, which is a term much larger than homogenous nu-

ACPD
10, 12907–12952, 2010

cleation, is also substantially suppressed, as shown in Fig. 7b. It is apparent that this suppression of homogeneous droplet freezing is related to the enhanced heterogeneous droplet freezing in contact and immersion modes. With the suppression of homogeneous freezing and nucleation in Case D, especially the former, ice hydrometeors of smaller sizes decrease accordingly (Fig. 4a) after 25 min when homogeneous nucleation occurs. The depositional growth of ice phase particles produced by heterogeneous processes in Case D cause the droplets to grow slower and to have smaller size.

As also shown in Fig. 4, the pattern of size spectrum changes of the mixing ratio of ice hydrometeors is similar to that of number concentration. They are in agreement with the observational study of Min et al. (2009) who found that precipitating hydrometeors shift to smaller sizes. The above analysis confirms that the sizes of ice hydrometeors were reduced because of the numerous ice particles introduced by heterogeneous nucleation.

The size and mass distributions of graupel particles were also modified due to the presence of dust. A similar analysis to that of Fig. 4 for the graupel particles confirmed that during the convection phase (25–30 min) the masses of large graupel particles have been decreased in the dust case. This result is explained by the reduction of drop size and mass in the dust case (Fig. 6). As a result, graupel growth from collision between graupel and drops decreased. However, for the dust case the number and mass of graupel particles increase at all size spectrum at later stages due to continuous contact freezing of drops (Fig. 3) and enhancement of sedimentation (Fig. 11).

3.3 Dynamical response

van den Heever et al. (2006) simulated the aerosol effects, including dust, on tropical convections in the Florida peninsula. Their results suggested that vertical updraft is significantly stronger in the presence of mineral dust. Figure 8 compares the vertical velocities of Cases F and D for time evolution between 10–39 min at 6–10.8 km and vertical profile at convective core. The convective updraft significantly increases until

ACPD
10, 12907–12952, 2010

30 min, with peak value near 25 min. The vertical profile shows that the maximum updraft enhancement occurred near 10 km.

The increase of updraft velocity is evidently related to the enhanced ice depositional heating (Fig. 5). Given the facts that saturation over ice is smaller than over water and there is additional frozen heat releases associated with droplets freezing, the growth of ice hydrometeors should have greater potential to release latent heat.

Meanwhile, ice hydrometeors generated by heterogeneous ice nucleation should also slightly increase the releasing of latent heat under ice saturation. On the other hand, it is expected that drop condensational heating is suppressed due to the freezing-reduced mixing ratio of drops (not shown). Overall, the change of total latent heat in the deep convection is dominated by that of ice depositional heating. The largest change in the total latent heat at levels of 6–10.8 km occurs around 25 min, when the convection develops into its peak with maximum updraft near 9 km. This result suggests that the difference in saturation between water and ice is a major reason for the latent heat release because the difference in saturation is increased with decreasing temperature until −80 °C. It is also clear that the enhancement of the updraft velocity in turn further strengthens the ice depositional and drop condensational latent heat releases by transporting more water vapor. Ultimately the process terminates when the available water vapor cannot sustain the feedback near 27 min, when both the updraft and deposition in Case D become weaker than that of Case F.

3.4 Cloud top change

In addition to the change in size of ice hydrometeors, dust also affects the cloud vertical structure. These effects eventually influence the radiative balance and thus have potential effects on climate (Min and Li, 2010a). For tropical deep convection, the anvils have larger radiation impact than the convective core because of their much larger spatial coverage. Therefore we mainly focused on the dust effects on cloud change in the stratiform precipitating stage. Figure 9 shows the difference of 40–100 min averaged ice hydrometeors between Cases D and F.

ACPD
10, 12907–12952, 2010

There is a substantial increase in the ice hydrometeors at levels below 10.2 km, and below 13.2 km at center of domain where convective core resided during convective precipitating stage. The increase below 10.2 km is the result of heterogeneous nucleation and freezing and vertical transport of ice hydrometeors. On the other hand, the small increase above 10.2 km should be related to the vertical transport of ice hydrometeors, which is strengthened by the enhancement of updraft velocity.

Another important feature shown in Fig. 9 is the considerable decrease of ice hydrometeors on both sides of convective core above 10.2 km. The dominant process to the decrease is the suppressed homogeneous droplet freezing nucleation while homogeneous nucleation also has contribution but is a minor one (Fig. 7a and b). The decreasing ice mixing ratio cloud had centers between 10.8 and 13 km. There are two reasons for explaining the formation of negative centers. First, at these altitudes homogeneous droplet freezing and nucleation begin to be activated. Second, the reduced moisture supply due to enhanced consumption by ice deposition transported from lower altitudes has the largest effects at these altitudes, as shown in Fig. 6. These simulation results comply with the findings in the observational studies of Min et al. (2009) and Min and Li (2010a) that suggested that dust lower the ice cloud top height.

3.5 Precipitation and precipitating rate vertical profile

With strong vertical updraft, drop condensation and ice deposition, tropical deep convections bring large amount of water vapor and cloud condensates to the tropopause, and release latent heat to the upper troposphere. As a consequence of these processes, precipitation is frequently associated with tropical deep convection, and therefore is a crucial indicator in the global hydrological cycle and energy budget.

Figure 10a shows the surface precipitation rates for Cases F and D in the domain. It is clear that mineral dust suppresses surface precipitation in the convective precipitating stage, with about 20% deficit in the peak precipitation rate at around 30 min. On the other hand, surface precipitation is significantly enhanced in the stratiform precipitating stage. For the net effect, dust suppresses the surface precipitation. The quantitative

ACPD
10, 12907–12952, 2010

statistics will be provided in Sect. 4.

The vertical structure of precipitation is an important measure of convective heating. Figure 10b shows the time variation of vertical profiles of percentage difference in the total precipitating rate (liquid+ice) between Cases D and F in the domain. The evolution of the difference in precipitation shows similar characteristics as surface precipitation.

During the convective precipitating stage, mineral dust significantly suppresses the precipitation below 11 km, with maximum suppression above 25% below 7.5 km. During the stratiform precipitating stage, the precipitating rate is increased by up to more than 50%, starting from lower stratosphere around 12 km at the late convective precipitating stage. After 50 min, the pattern of difference shows fluctuations, with enhanced precipitating rate above 8 km and weak suppressed precipitating rate below 8 km.

In agreement with the analysis of Min et al. (2009), the suppressed peak of precipitating rate is the combined results of the reduced sedimentation and collection efficiency. Figure 11 shows the height-time cross-section of sedimentation. Before 30 min, sedimentation decreases due to the reduced sizes of precipitating ice hydrometeors and the enhanced updraft velocity. However, it increases after 40 min. The peak of collection rate, as shown in Fig. 12, is reduced by nearly 18%, compared to the peak value in Case F. This peak reduction occurs when the large graupels form, which is critical to the suppressed surface precipitation. The increased graupel number concentration due to heterogeneous freezing processes is responsible for the reduction of the collection of ice hydrometeors for large size graupel.

Note that, nevertheless, since the mineral dust induces the ice hydrometeors in the convection through heterogeneous nucleation earlier, the collection process occurs earlier in Case D. On the other hand, the increased precipitation at 12 km is related to the enhanced depositional growth before 35 min (as shown in Fig. 5).

ACPD
10, 12907–12952, 2010

4 Results with initial horizontal wind

The horizontal wind used in Cases FU and DU, (Fig. 1b), has a strong vertical shear. In the troposphere, easterly (to the left) prevailed below 10.8 km, with maximum around 7.7 and 6.3 m s^{-1} at 4.3 and 9.6 km, respectively. In the stratosphere, there was stronger westerly of 14.7 m s^{-1} at 13.2 km. As shown below, the vertical shear in the horizontal winds can weaken the development of the deep convection.

The cases simulated with horizontal wind are more realistic than the pairs without horizontal wind. The impact of dust aerosol on deep convective cloud is similar to the description provided in Sect. 3. For example, Fig. 13 shows the ice cloud mixing ratio difference between Cases DU and FU during stratiform stage and demonstrates the cloud top change. The cloud top generally decreases above 11 km, but increases below the altitudes. The pattern of the difference is like a twisted cloud of the results without horizontal wind that is shown in Fig. 9, with the lower part leaning to the left and the upper part to the right. This is apparently the result of cloud horizontal movements associated with the horizontal wind.

Figure 14 shows the domain surface precipitation in Cases FU and DU. The convective precipitation is substantially suppressed in Case DU by about 1/3, and the stratiform precipitation is moderately enhanced.

To understand the simulations in terms of the observed quantity, we plotted the simulated radar reflectivity in DBZ of Cases F, D, FU and FD in Fig. 15. The dust cases (right panels) have apparent enhancement of echo after 35 min at levels above 6 km. This feature is due to the slow depositional growth of ice particles associated with increased heterogeneous nucleation. This result is in good agreement with the mechanism as revealed in the observational study Min et al. (2009; Fig. 2). On the other hand, the echo of DBZ during the convective precipitating stage is substantially weakened in these dust cases, which is the result of reduced collection coefficient. A slight increase in the reflectivity also occurs above 5 km before 22 min. The DBZ changes due to dust in the convective precipitating stage is not clearly discerned in Min et al. (2009) because

ACPD
10, 12907–12952, 2010

the dynamical situation in the dust and dust-free sector are different, and the minimum threshold of TRMM precipitation radar is 17 DBZ. Finally, Fig. 15 shows that the cases with horizontal winds have a relatively weaker convection, which is also in agreement with observational studies (Dunion and Velden, 2004).

In Tables 2 and 3, we calculated several statistics of the changes induced by mineral dust. The two cases with horizontal winds show larger impacts, except for the enhancement of stratiform precipitation (Rs), which might be due to the choice of horizontal grids for statistics. Clouds move outsides the domain (grid points 100–200) and eventually are merged with the clouds that are formed at the lateral boundaries. These amplified impacts in Cases DU and FU should be related to cloud horizontal movements. With the movements, more IN is available for the heterogeneous nucleation and freezing than that for the erect cloud body that relies on the vertical transport of dust aerosol by updrafts. Besides, the convective core starts to move away from the domain center at 12 min. The thermal forcing at the center, which we applied in the simulations, has less limitation on the cloud development, and thus would contribute to the amplification.

Among the percentage changes in Tables 2 and 3, it is noted that the largest impact of mineral dust is on the number concentration of ice hydrometeors, which is more than tripled in Case DU. The ice water path in the middle and upper troposphere (5.1–10.8 km) is also substantially increased by almost 1/2. The total column water path, total surface precipitation and convective updraft are moderately changed. There are small increases in cloud cover, which may be the result of enhanced updraft that enlarges the cloud body.

5 Conclusion and discussion

In this study, the SAL mineral dust impacts on tropical deep convection is investigated using the Tel Aviv detailed cloud resolving model with spectral solutions of the aerosol and cloud condensates. In agreement with the observational analysis of dust effects by

ACPD
10, 12907–12952, 2010

Min et al. (2009) and Min and Li (2010a), the simulations suggested that dust aerosol substantially affect both the cloud microphysics and dynamics.

It was shown that mineral dust not only increases the number concentration of ice hydrometeors at temperatures warmer than −40 °C, shifts the spectrum of precipitating size particles to the lower side, modifies the graupel production, suppresses the heavy precipitation and increase light precipitation, but also lowers the height of ice cloud top. The updraft velocity of convection is also stronger during the convective precipitating stage.

These dust-induced changes in deep clouds may have profound implications on the global radiative budget as well as hydrological cycle. With warmer cloud temperature, the lowered cloud top will increase the outgoing longwave radiation, and therefore cools the atmospheric-earth system (Min and Li, 2010a). In addition, the increase in the reflectivity associated with larger cloud optical depth as well as the cloud cover will also have cooling effects. Both of these cooling effects will suppress the convective activity. In contrast, the enhanced convective updraft will mitigate these radiation effects. The integrated impacts cannot be explored using the current DCRM, but can be evaluated by climate models. These models include the interaction of cloud microphysics, radiation, convection and surface heat fluxes.

In this study, the model sensitivity of dust impacts might be affected by the thermal forcing, especially for its influence on updraft velocity. As the thermal forcing maintains the convective updraft in the dust-free simulation, the intensification in updraft velocity might be stronger in real case. However, dust-related ice nucleation and freezing as well as the cloud formation could be exaggerated at altitudes with the largest gradient of thermal forcing. In addition to the single dust event simulation with hypothesis that dust acts only as ice nucleus, the dust impacts needs to be quantified in our future studies under various atmospheric conditions. In particular, the competition for water vapor between heterogeneous and homogeneous freezing and nucleation depends strongly on the water vapor supply associated with convective strength and middle level moisture abundance.

ACPD
10, 12907–12952, 2010

The competition for super cooled water between heterogeneous and homogeneous freezing is also related to the updraft velocity. The resultant cloud top change will be modulated by the vertical transport of ice hydrometeors nucleated at middle levels. In Part 2, we shall address the issues on dust compositions of dust aerosols and atmospheric condition. Specifically, sensitivity experiments will be conducted for partially soluble dust aerosols that act as CCN, GCCN as well as their mixtures with IN. Furthermore, sensitivity of dust impacts under situations of dry SAL environment in the middle troposphere will also be discussed.

Acknowledgements. This research was supported by the Office of Science (BER), US Department of Energy, Grant DE-FG02-03ER63531, and by the NOAA Educational Partnership Program with Minority Serving Institutions (EPP/MSI) under cooperative agreements NA17AE1625 and NA17AE1623.

References

Albrecht, B. A.: Aerosols, cloud microphysics, and fractional cloudiness. Science, 245, 1227–1230, 1989.

Bigg, E. K.: The supercooling of water, Proc. Phys. Soc. London, 66B, 688–694, 1953.

Carlson, T. N. and Prospero, J. M.: The large-scale movement of Saharan Air outbreaks over the northern equatorial Atlantic, J. Appl. Meteorol., 11, 283–297, 1972.

DeMott, P. J., Kreidenweis, S. M., Twohy, C. H., and Rogers, D. C.: Ice nuclei variability and ice formation in mixed-phase clouds, Sixteenth ARM Science Team Meeting Proceedings, Albuquerque, NM, 1–8, 2006.

DeMott, P. J., Meyers, M. P., and Cotton, W. R.: Parameterization and impact of ice initiation processes relevant to numerical model simulation of cirrus clouds, J. Atmos. Sci., 51, 77–90, 1994.

DeMott, P. J., Sassen, K., Poellot, M. R., Baumgardner, D., Rogers, D. C., Brooks, S. D., Prenni, A. J., and Kreidenweis, S. M.: African dust aerosols as atmospheric ice nuclei, Geophys. Res. Lett., 30, 1732–1735, 2003.

Dunion, J. P. and Velden, C. S.: The Impact of the Saharan Air Layer on Atlantic Tropical Cyclone Activity, B. Am. Meteorol. Soc., 85, 353–365, 2004.

ACPD

10, 12907–12952, 2010

Ginoux, P., Prospero, J., and Terres, O.: Long-term simulation of global dust distribution with the GOCART model: Correlation with North Atlantic Oscillation, Environ. Model. Softw., 19, 113–128, 2004.
Hallet, J. and Mossop, S. C.: Production of secondary ice crystals during the riming process, Nature, 249, 26–28, 1974.
Heymsfield, A. J. and Miloshevich, L. M.: Homogeneous ice nucleation and supercooled liquid water in orographic wave clouds, J. Atmos. Sci., 50, 2335–2353, 1993.
Houghton, J. T., Ding, Y., Griggs, D. J., Noguer, M., van der Linden, P. J., and Xiaosu, D.: Climate Change 2001: The Scientific Basis – Contribution of Working Group I to the Third Assessment Report of the Intergovernmental Panel on Climate Change (IPCC), Cambridge University Press, UK, 944 pp., 2001.
Houze, R. A.: Cloud Dynamics, Academic Press, 573 pp., 1993.
Karyampudi, V. M. and Carlson, T. N.: Analysis and Numerical Simulations of the Saharan Air Layer and Its Effect on Easterly Wave Disturbances, J. Atmos. Sci., 45, 3102–3136, 1988.
Khain, A., Lynn, B., and Dudhia, J.: Aerosol effects on intensity of landfalling hurricanes as seen from simulations with WRF model with spectral bin microphysics, J. Atmos. Sci., doi:10.1175/2009JAS3210.1, in press, 2009.
Koop, T., Ng, H. P., Molina, L. T., and Molina, M. J.: A new optical technique to study aerosol phase transitions: The nucleation of ice from H_2SO_4 aerosols, J. Phys. Chem., 102A, 8924–8931, 1998.
Levin, Z., Ganor, E., and Gladstein, V.: The effects of desert particles coated with sulfate on the rain formation in the eastern Mediterranean, J. Appl. Meteorol., 35, 1511–1523, 1996.
Levin, Z., Teller, A., Ganor, E., and Yin, Y.: On the interactions of mineral dust, sea salt particles and clouds – Measurements and modeling study from the MEIDEX campaign, J. Geophys. Res., 110, D20202, doi:10.1029/2005JD005810, 2005.
Liu, X. and Penner, J. E.: Ice nucleation parameterization for global models. Meteor. Z., 14, 499–514, 2005.
Liu, X., Penner, J. E., Ghan, S. J., and Wang, M.: Inclusion of Ice Microphysics in the NCAR Community Atmospheric Model Version 3 (CAM3), J. Climate, 20, 4526–4547, 2007.
Lohmann, U. and Diehl, K.: Sensitivity Studies of the Importance of Dust Ice Nuclei for the Indirect Aerosol Effect on Stratiform Mixed-Phase Clouds, J. Atmos. Sci., 63, 968–982, 2006.
Lohmann, U.: Possible aerosol effects on ice clouds via contact nucleation, J. Atmos. Sci., 59, 647–656, 2002.

ACPD
10, 12907–12952, 2010

Meyers, M. P., Demott, P. J., and Cotton, W. R.: New primary ice nucleation parameterizations in an explicit cloud model, J. Appl. Meteor., 31, 708–721, 1992.
Min, Q., Li, R., Lin, B., Joseph, E., Wang, S., Hu, Y., Morris, V., and Chang, F.: Evidence of mineral dust altering cloud microphysics and precipitation, Atmos. Chem. Phys., 9, 3223–3231, doi:10.5194/acp-9-3223-2009, 2009.
Min, Q. and Li, R.: Longwave indirect effect of mineral dusts on ice clouds, Atmos. Chem. Phys. Discuss., 10, 763–783, doi:10.5194/acpd-10-763-2010, 2010a.
Min, Q., Gong, W., Joseph, E., and Morris, V.: Detailed cloud resolving model simulations of the impacts of Saharan air layer dust on tropical deep convection – Part 2: Sensitivities to dust sulfate coating, dust loading, and relative humidity, to be submitted to Atmos. Chem. Phys. Discuss., 2010b.
Morris, V., Clemente-Colon, P., Nalli, N. R., Joseph, E., Armstrong, R. A., Detres, Y., Goldberg, M. D., Minnett, P. J., and Lumpkin, R.: Measuring Trans-Atlantic Aerosol Transport from Africa, EOS, Transactions, AGU, 87, 565–571, 2006.
Muhlbauer, A. and Lohmann, U.: Sensitivity Studies of Aerosol–Cloud Interactions in Mixed-Phase Orographic Precipitation, J. Atmos. Sci., 66, 2517–2538, 2009.
Posselt, R. and Lohmann, U.: Sensitivity of the total anthropogenic aerosol effect to the treatment of rain in a global climate model, Geophys. Res. Lett., 36, L02805, doi:10.1029/2008GL035796, 2009.
Prospero, J. M. and Carlson, T. N.: Radon-222 in the north Atlantic trade winds: Its relationship to dust transport from Africa, Science, 167, 974–977, 1970.
Pruppacher, H. R. and Klett, J. D.: Microphysics of Clouds and Precipitation, 2nd ed, Kluwer Academic, 954 pp., 1997.
Reisin, T., Levin, Z., and Tzivion, S.: Rain production in convective clouds as simulated in an axisymmetric model with detailed microphysics, Part I: Description of the model, J. Atmos. Sci., 53, 497–519, 1996.
Reisin, T., Yin, Y., Levin, Z., and Tzivion, S.: Development of giant drops and high reflectivity cores in Hawaiian clouds: numerical simulations using a kinetic model with detailed microphysics, Atmos. Res., 45, 275–297, 1998.
Rosenfeld, D., Rudich, Y., and Lahav, R.: Desert dust suppressing precipitation: A possible desertification feedback loop, P. Natl. Acad. Sci. USA, 98, 5975–5980, 2001.
Sassen, K., Demott, P. J., Prospero, J. M., and Poellet, M. R.: Saharan Dust storms and indirect aerosol effects on clouds: CRYSTAL-FACE Results, Geophys. Res. Lett., 30, 1633–1636,

ACPD
10, 12907–12952, 2010

2003.
Schütz, L., Jaenicke, R., and Petrick, H.: Saharan dust transport over the North Atlantic Ocean. Desert Dust: Origin, Characteristics and Effect on Man. T. L. Pe'we', Ed., Geological Society of America, 87–100, 1981.
Semeniuk, T. A., Wise, M. E., Martin, S. T., Russell, L. M., and Buseck, P. R.: Water uptake characteristics of individual atmospheric particles having coatings, Atmos. Environ., 41, 6225–6235, 2007.
Teller, A. and Levin, Z.: The effects of aerosols on precipitation and dimensions of subtropical clouds: a sensitivity study using a numerical cloud model, Atmos. Chem. Phys., 6, 67–80, doi:10.5194/acp-6-67-2006, 2006.
Trochkine, D., Iwasaka Y., Matsuki, A., Yamada, M., Kim, Y.-S., Nagatani, T., Zhang, D., Shi, G.-Y., and Shen, Z.: Mineral aerosol particles collected in Dunhuang, China and their comparison with chemically modified particles collected over Japan. J. Geophys. Res, 108, 8642, doi:10.1029/2002JD003268, 2003.
Twomey, S.: The influence of pollution on the shortwave albedo of clouds, J. Atmos. Sci., 34, 1149–1152, 1977.
Tzivion, S., Feingold, G., and Levin, Z.: A efficient numerical solution to the stochastic collection equation, J. Atmos. Sci., 44, 3139–3149, 1987.
Van Den Heever, S. C., Carrio, G. G., Cotton, W. R., DeMott, P. J., and Prenni, A. J.: Impacts of Nucleating Aerosol on Florida Storms. Part I: Mesoscale Simulations, J. Atmos. Sci., 63, 1752–1775, 2006.
Wu, X., and Moncrieff, M.: Collective Effects of Organized Convection and Their Approximation in General Circulation Models, J. Atmos. Sci., 53, 1477–1495, 1996.
Yin, Y., Levin, Z., Reisin, T. G., and Tzivion, S.: The effect of giant cloud condensation nuclei on the development of precipitation in convective clouds – A numerical study, Atmos. Res., 53, 91–116, 2000.
Yin, Y., Carslaw, K. S., and Feingold, G.: Vertical transport and processing of aerosols in a mixed phase convective cloud and the feedback on cloud development, Q. J. Roy. Meteorol. Soc., 131, 221–246, 2005.
Yin, Y. and Chen, L.: The effects of heating by transported dust layers on cloud and precipitation: a numerical study, Atmos. Chem. Phys., 7, 3497–3505, doi:10.5194/acp-7-3497-2007, 2007.

ACPD
10, 12907–12952, 2010

Table 1. March 2004 ship observed aerosol number for different sizes on dust-free and dust days.

Radius (micron)	0.3–0.5 cm^{-3}	0.5–1 cm^{-3}	1–5 cm^{-3}	5–10 cm^{-3}	10–25 cm^{-3}	25 cm^{-3}
Dust-Free	108.6	10.5	2.36	0.1029	3.0E-4	5.5E-8
Dust	87.32	34.7	7.557	0.3537	1.45E-3	7.41E-6

ACPD
10, 12907–12952, 2010

Table 2. Simulated total (R), convective (Rc), and stratiform (Rs) precipitation (mm/hour) in the domain (grid 100–200). Numbers in the parenthesis are percentage changes between dust and dust-free runs.

Case	R (mm/hour)	Rc (mm/hour)	Rs (mm/hour)
F	71.08	144.85	21.90
D	61.25 (−13.82)	110.26 (−23.87%)	28.57 (30.45%)
FU	48.82	96.36	17.13
DU	38.10 (−21.95%)	65.39 (−32.17%)	19.90 (16.17%)

ACPD
10, 12907–12952, 2010

Table 3. Same as in Table 2, but for heterogeneous nucleation level updraft velocity (W), column ice (ICWP) and total cloud water paths (TCWP), heterogeneous nucleation level (HINC; 5.1–10.8 km) and total (TINC) ice particles number concentrations, and cloud spatial coverage (C). The updraft velocity W is calculated between 10 and 35 min, and grid 145–155. Other quantities are averaged over 100 min in the domain.

Case	W (m s^{-1})	ICWP (kg m^{-2})	TCWP (kg m^{-2})	HINC (m^{-3})	TINC (m^{-3})
F	4.80	8.18	13.10	4.61	5.01
D	5.20 (8.33%)	10.30 (25.92%)	14.70 (12.21%)	13.93 (202.17%)	8.53 (67.25%)
FU	2.46	3.90	8.08	3.67	3.70
DU	2.86 (16.26%)	5.81 (48.97%)	9.61 (18.94%)	15.54 (323.43%)	7.74 (109.19%)

ACPD
10, 12907–12952, 2010

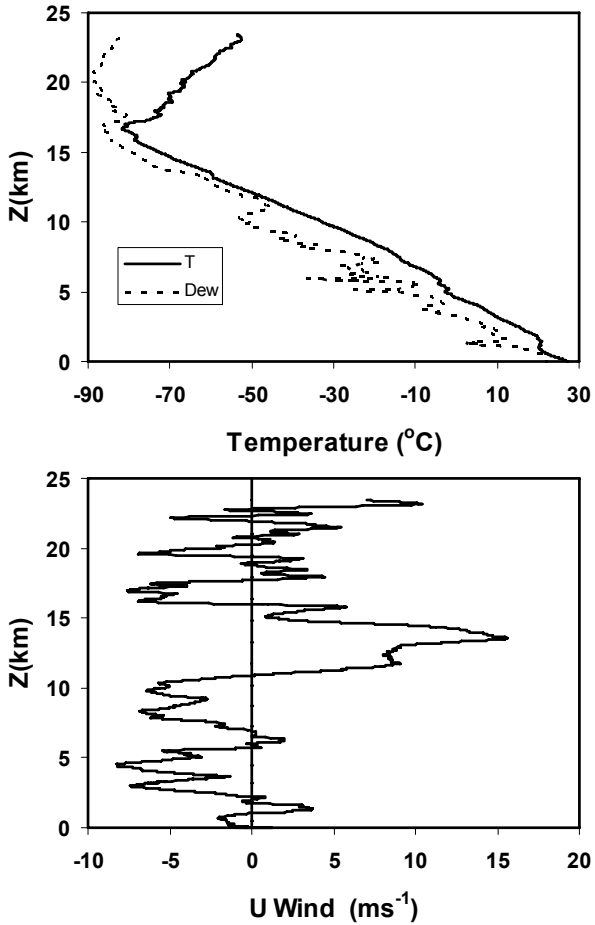

Fig. 1. Initial vertical profiles of **(a)** temperature (solid; °C) and dew point (dashed); and **(b)** u wind (m/s) observed at −23° W and 9° N on 19:31 UTC 01, July 2006.

ACPD
10, 12907–12952, 2010

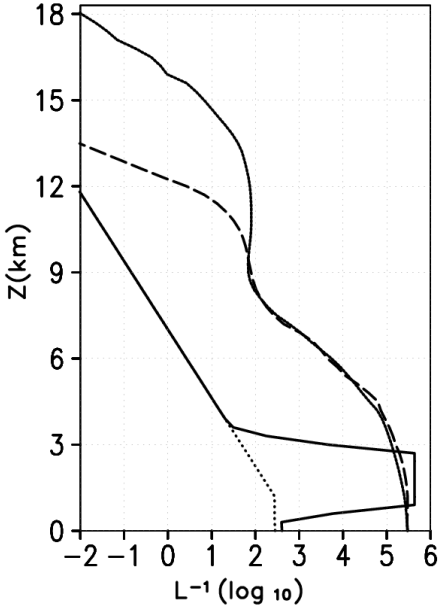

Fig. 2. Averaged (grid 100–200) vertical profiles of Ice Nuclei (IN; in 1/litre of logarithm scale) for Cases F (dot; initial) and D. Solid: initial; long dashed: 32 min, and dashed: 100 min.

ACPD
10, 12907–12952, 2010

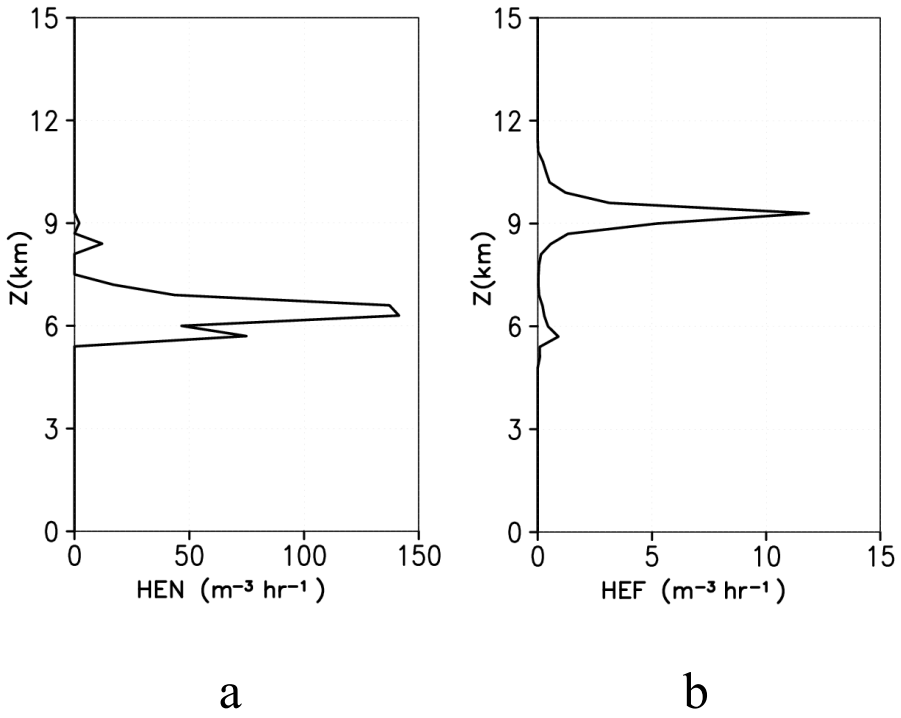

Fig. 3. Averaged (grid 140–160; 1–40 min) vertical profiles of **(a)** heterogeneous ice number concentration nucleation rate (HEN); and **(b)** heterogeneous ice freezing rate (HEF) for Case D.

ACPD
10, 12907–12952, 2010

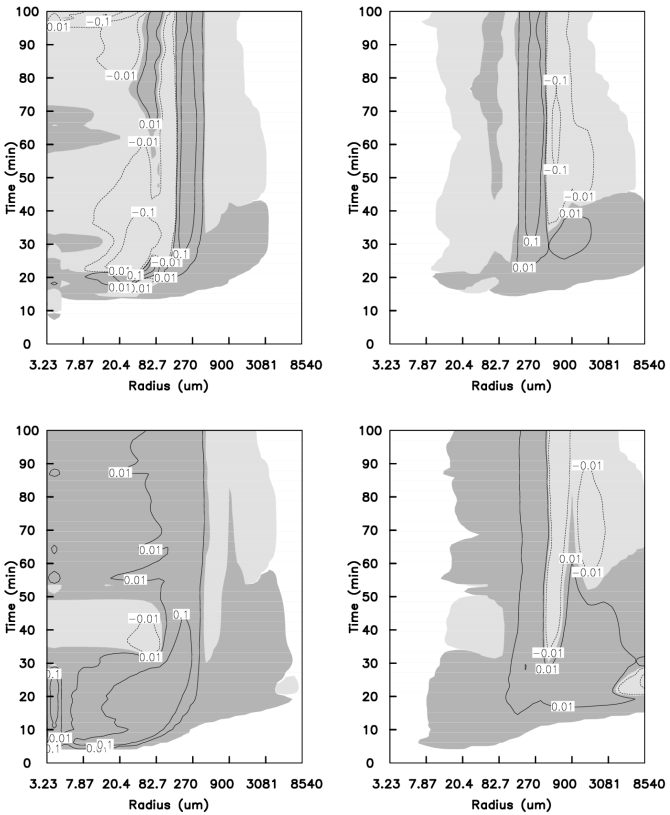

Fig. 4. Time evolution (y axis; in minutes) of ice phase condensates size (X axis; in μm) distribution change due to dust. Statistics are calculated over grid 100–200, for 11.1–14.0 km (upper panels) and for 6.0–10.8 km (lower panels). Left panels are number concentration; right are mass concentration. Dark and light shaded area is respectively for positive and negative changes. Contour of −0.01 and 0.01 1/litre/μm and g/kg/μm are plotted respectively for number concentration and mixing ratio.

ACPD
10, 12907–12952, 2010

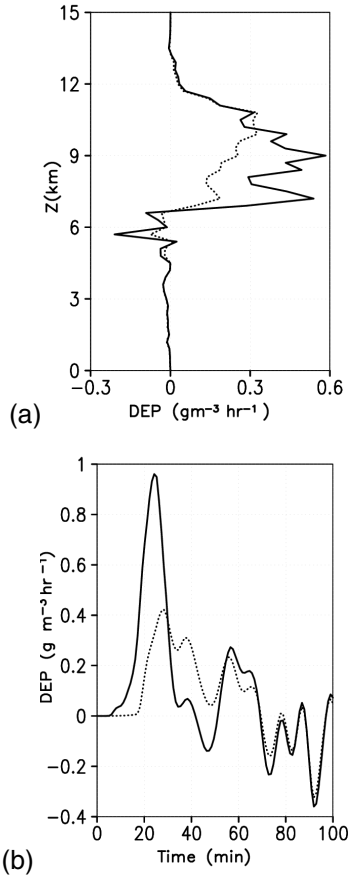

Fig. 5. Ice deposition growth rate vertical profiles before 39 min **(a)** and time evolution between 6–10.8 km **(b)** at convective core (grid 140–160). Dot is for Case F and solid for Case D.

ACPD
10, 12907–12952, 2010

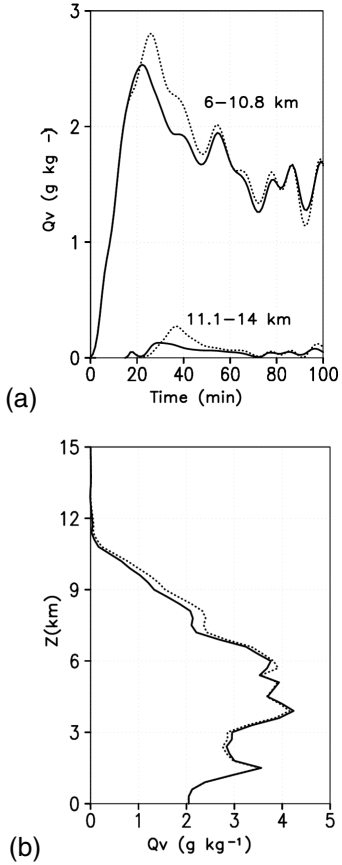

Fig. 6. Water vapor mixing ratio perturbation time evolution between 6–10.8 km and between 11.1–14 km **(a)**; and vertical profiles between 20–60 min **(b)** at convective core (grid 140–160). Dot is for Case F and solid for Case D, respectively.

ACPD
10, 12907–12952, 2010

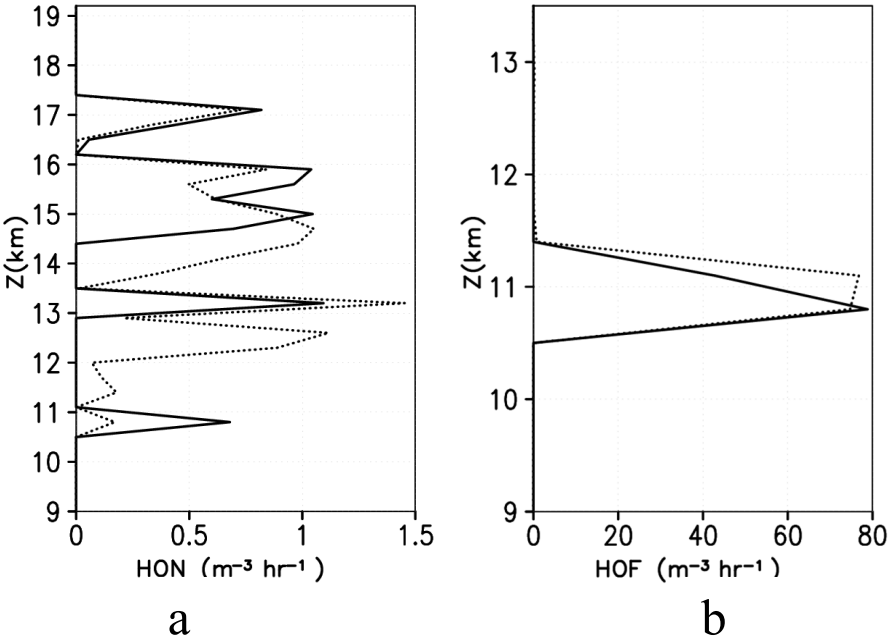

Fig. 7. Vertical profiles of **(a)** homogeneous ice number concentration nucleation rate (HON; in $1/m^3/h$); and **(b)** homogeneous droplet number concentration freezing rate (HOF; in $1/m^3/h$) at convective core (grid 140–160) for Cases F (dot) and D (solid) averaged at 1–100 min.

ACPD
10, 12907–12952, 2010

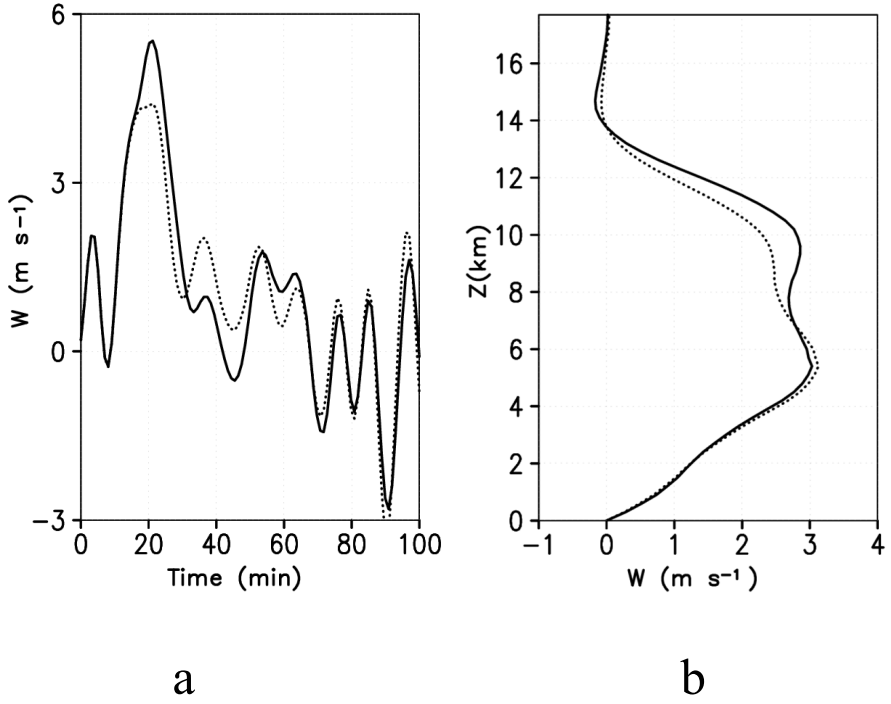

Fig. 8. Vertical velocity (m/s) time evolution between 6–10.8 km **(a)** and vertical profiles between 10–39 min **(b)** at convective core (grid 140–160). Dot is for Case F and solid for Case D, respectively.

ACPD
10, 12907–12952, 2010

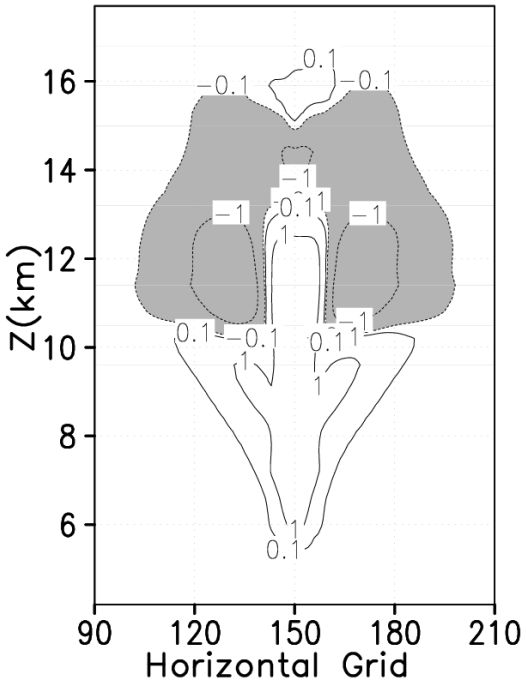

Fig. 9. Dust effects on ice phase condensates mixing ratio. Statistics are calculated between 40–100 min. Contour levels are −1, −0.1, 0.1 and 1 μg/kg. Light and dark shaded areas is −0.1 and −1 μg/kg, respectively.

ACPD
10, 12907–12952, 2010

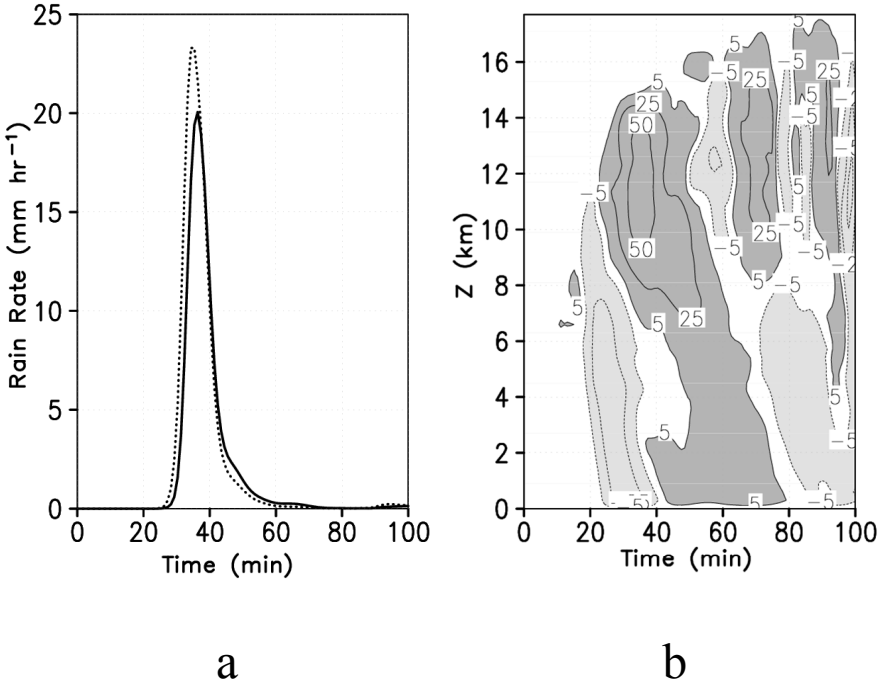

Fig. 10. (a) Surface precipitation rate (mm/hour) in the domain (grid 100–200). Dot is for Case F and solid for Case D, respectively. **(b)** Percentage changes (percent) in rain rate vertical profile in the domain (grid 100–200). Contours are at −50, −25, −5, 5, 25, and 50%. Light shaded area: <−5%; darker shaded area: >5%.

ACPD
10, 12907–12952, 2010

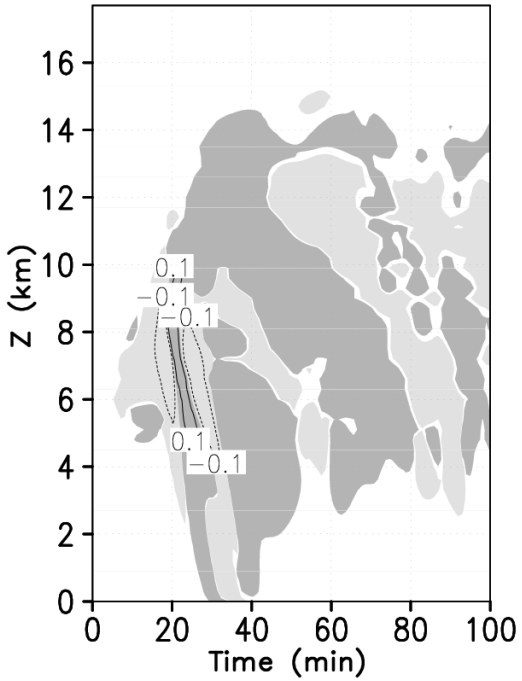

Fig. 11. Time-height evolution of ice phase hydrometeors sedimentation rate change in the domain (grid 100–200). Dot is for Case F and solid for Case D, respectively. Light shaded area <-0.001 g/m^3/h, darker >0.001 g/m^3/h. Two contour levels of -0.1 and 0.1 g/m^3/h are plotted.

ACPD
10, 12907–12952, 2010

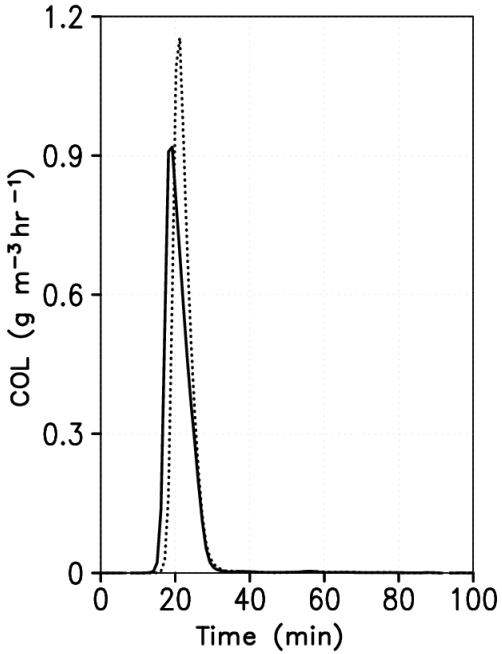

Fig. 12. Ice collection rate time evolution between 6–10.8 km in the domain (grid 100–200). Dot is for Case F and solid for Case D, respectively.

ACPD
10, 12907–12952, 2010

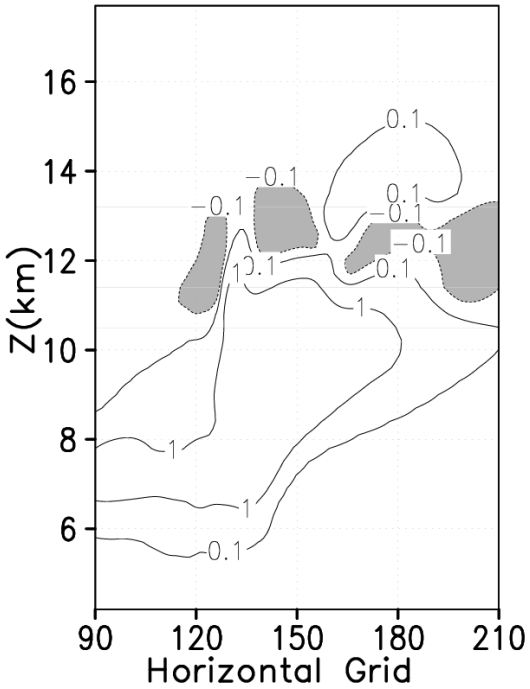

Fig. 13. Same as in Fig. 9, except for cases with horizontal winds. Contour levels are −0.1, 0.1 and 1 μg/kg. Shaded area is −0.1 μg/kg.

ACPD
10, 12907–12952, 2010

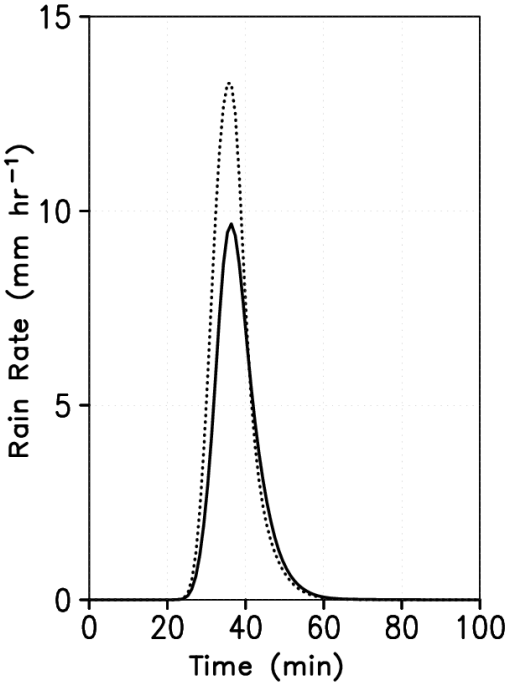

Fig. 14. Same as in Fig. 10, except for Cases with horizontal winds.

ACPD
10, 12907–12952, 2010

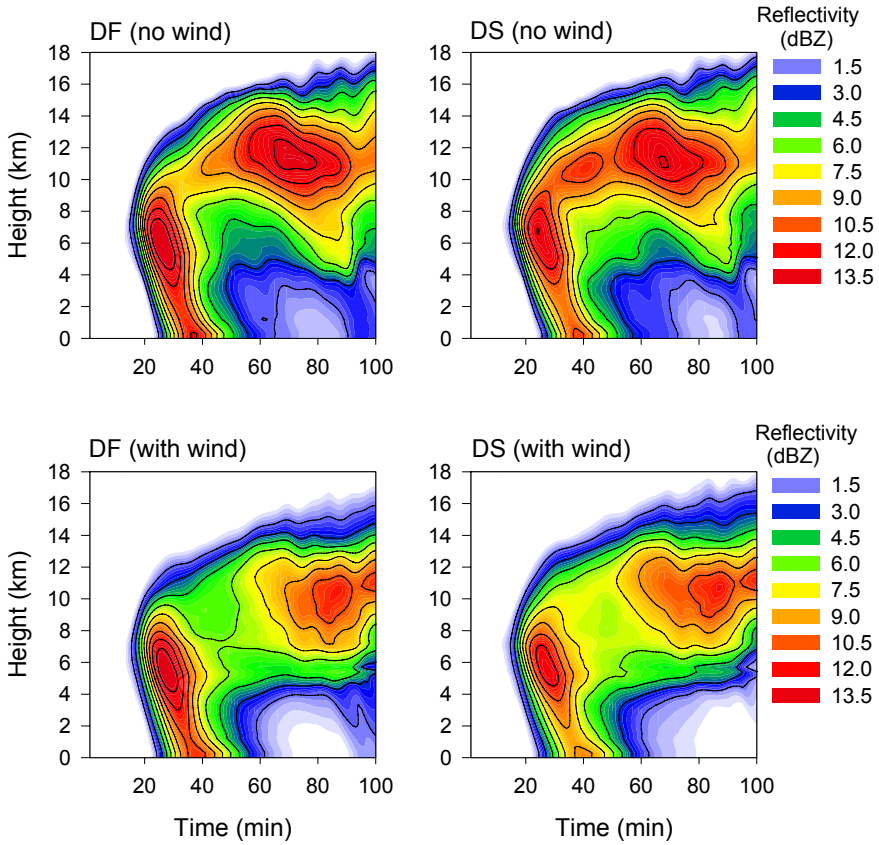

Fig. 15. Time-height distribution of DBZ (radar reflectivity) simulated by Cases F (upper left panel), D (upper right panel), FU (lower left panel) and FD (lower right panel).

ACPD
10, 12907–12952, 2010